Opto-Electronic Advances

ISSN 2096-4579 CN 51-1781/TN

Luminescence regulation of Sb^{3+} in 0D hybrid metal halides by hydrogen bond network for optical anti-counterfeiting

Dehai Liang, Saif M. H. Qaid, Xin Yang, Shuangyi Zhao, Binbin Luo, Wensi Cai, Qingkai Qian and Zhigang Zang

Citation: Liang DH, Qaid SMH, Yang X, et al. Luminescence regulation of Sb^{3+} in 0D hybrid metal halides by hydrogen bond network for optical anti-counterfeiting. *Opto-Electron Adv* **7**, 230197(2024).

https://doi.org/10.29026/oea.2024.230197

Received: 27 October 2023; Accepted: 5 January 2024; Published online: 13 March 2024

Opto-Electronic Advances

Article

March 2024, Vol. 7, No. 3

DOI: 10.29026/oea.2024.230197

Luminescence regulation of Sb^{3+} in 0D hybrid metal halides by hydrogen bond network for optical anti-counterfeiting

Dehai Liang[1], Saif M. H. Qaid[2], Xin Yang[4]*, Shuangyi Zhao[1]*, Binbin Luo[3]*, Wensi Cai[1], Qingkai Qian[1] and Zhigang Zang[1]*

The Sb^{3+} doping strategy has been proven to be an effective way to regulate the band gap and improve the photophysical properties of organic-inorganic hybrid metal halides (OIHMHs). However, the emission of Sb^{3+} ions in OIHMHs is primarily confined to the low energy region, resulting in yellow or red emissions. To date, there are few reports about green emission of Sb^{3+}-doped OIHMHs. Here, we present a novel approach for regulating the luminescence of Sb^{3+} ions in 0D $C_{10}H_{22}N_6InCl_7{\cdot}H_2O$ via hydrogen bond network, in which water molecules act as agents for hydrogen bonding. Sb^{3+}-doped $C_{10}H_{22}N_6InCl_7{\cdot}H_2O$ shows a broadband green emission peaking at 540 nm and a high photoluminescence quantum yield (PLQY) of 80%. It is found that the intense green emission stems from the radiative recombination of the self-trapped excitons (STEs). Upon removal of water molecules with heat, $C_{10}H_{22}N_6In_{1-x}Sb_xCl_7$ generates yellow emission, attributed to the breaking of the hydrogen bond network and large structural distortions of excited state. Once water molecules are adsorbed by $C_{10}H_{22}N_6In_{1-x}Sb_xCl_7$, it can subsequently emit green light. This water-induced reversible emission switching is successfully used for optical security and information encryption. Our findings expand the understanding of how the local coordination structure influences the photophysical mechanism in Sb^{3+}-doped metal halides and provide a novel method to control the STEs emission.

Keywords: indium-based halides; Sb^{3+} doping; hydrogen bonding network; optical anti-counterfeiting

Liang DH, Qaid SMH, Yang X et al. Luminescence regulation of Sb^{3+} in 0D hybrid metal halides by hydrogen bond network for optical anti-counterfeiting. *Opto-Electron Adv* **7**, 230197 (2024).

Introduction

Organic-inorganic hybrid metal halides (OIHMHs) are emerging semiconductor materials that exhibit excellent optoelectronic properties, making them a particularly suitable choice for the development of optoelectronic devices, including lasers, scintillators, photodetectors and light emitting diodes (LEDs)[1–7]. In OIHMHs, the valence and conduction bands are primarily formed by the orbital hybridization between metal ions and halogen ions[8–14]. As a result, the optical properties of OIHMHs predominantly depend on the specie of metal and halogen ions[15,16].

[1]Key Laboratory of Optoelectronic Technology & Systems (Ministry of Education), Chongqing University, Chongqing 400044, China; [2]Department of Physics & Astronomy, College of Sciences, King Saud University, P.O. Box 2455, Riyadh 11451, Saudi Arabia; [3]Department of Chemistry and Chemical Engineering, Key Laboratory for Preparation and Application of Ordered Structural Materials of Guangdong Province, Shantou University, Shantou 515063, China; [4]Department of Oil, Army Logistics Academy of PLA, Chongqing 401311, China.

*Correspondence: X Yang, E-mail: beyondyzs@126.com; SY Zhao, E-mail: shyzhao@cqu.edu.cn; BB Luo, E-mail: bbluo@stu.edu.cn; ZG Zang, E-mail: zangzg@cqu.edu.cn

Received: 27 October 2023; Accepted: 5 January 2024; Published online: 13 March 2024

Due to the typical $5s^2$ electron configuration of Sb^{3+}, Sb^{3+}-doping has been proven to be an effective method to tune the photophysical properties of OIHMHs by regulating the band structure of metal halides[17,18]. A series of Sb^{3+}-doped $(C_9H_{15}N_3)_2SnCl_8$ was reported by Liu et al. using the cooling crystallization method[19]. Upon excitation with ultraviolet (UV) light at room temperature, Sb^{3+}-doped $(C_9H_{15}N_3)_2SnCl_8$ displayed red emission centered at 688 nm as well as an increase of photoluminescence quantum yield (PLQY) from 1% to 17.84%, attributed to the enhancement of self-trapped excitons (STEs) emission of Sb^{3+} dopant. Zou *et al.* have reported a series of zero-dimensional (0D) hybrid metal halides based on Sb^{3+}-doped tin(IV) compounds, denoted as $(C_{13}H_{30}N)_2SnCl_6$:*x*%Sb[20]. Among these compounds, $(C_{13}H_{30}N)_2SnCl_6$:20%Sb exhibits a bright red emission with a PLQY of 80.98% when excited at 380 nm under room temperature. Apart from Sn(IV)-based halides, Sb^{3+} doping has also been employed to enhance the optical property of Cd-based and In-based metal halide. For example, Sb^{3+}-doped $[NH_3(CH_2)_4NH_3]CdBr_4$ exhibited an intense orange emission at approximately 640 nm[21]. This material demonstrated a large Stokes shift of approximately 1.33 eV and a full width at half-maximum (FWHM) of around 0.45 eV. Upon introducing 0.01% Sb doping, the PLQY of $[NH_3(CH_2)_4NH_3]CdBr_4$ approached near-unity, reaching approximately 97%. Furthermore, 0D MA_4InCl_7 [MA^+: $CH_3NH_3^+$] halides with varying doping levels of Sb^{3+} were prepared using a solvent evaporation method[22]. MA_4InCl_7 doped with Sb^{3+} exhibits a broadband yellow emission with a FWHM of 180 nm and a high PLQY of 84%. However, because 0D metal halides lead a large distortion of $[SbX_6]^{3-}$ in the excited states, the emission of Sb^{3+} ions in these cases is primarily located in yellow or red range. Compared to all inorganic metal halides, OIHMHs have a soft crystal lattice which is easy to lattice distortion. To date, there are few reports about green emission based on Sb^{3+} in hybrid metal halides. Thus, it is still a challenge to realize the green light emission from such Sb^{3+} doped OIHMHs.

In this work, a new strategy was proposed to control the luminescence of STEs in the inorganic clusters by tuning the hydrogen bond network in the crystal structure. 0D lead-free $C_{10}H_{22}N_6InCl_7{\cdot}H_2O$ and Sb^{3+}-doped $C_{10}H_{22}N_6InCl_7{\cdot}H_2O$ were synthesized using an anti-solvent diffusion method. The hydrogen bonding in $C_{10}H_{22}N_6InCl_7{\cdot}H_2O$ is mediated by water guest molecules to form a network of hydrogen bonds. When Sb^{3+} is introduced into the metal halides, Sb^{3+} doped $C_{10}H_{22}N_6InCl_7{\cdot}H_2O$ shows an intense broadband green emission peaking at 540 nm and a high PLQY of 80%. The strong electron-phonon coupling in the 0D crystalline structures of Sb^{3+} doped $C_{10}H_{22}N_6InCl_7{\cdot}H_2O$ is believed to result in broadband green light emission originating from STEs. The hydrogen bond network limits the structural distortion of the excited state of the inorganic cluster, which plays an important role in the green light emission of Sb^{3+} doped $C_{10}H_{22}N_6InCl_7{\cdot}H_2O$. However, breaking the hydrogen bond network with the help of heat causes Sb^{3+}-doped $C_{10}H_{22}N_6InCl_7$ to emit a yellow light. This reversible emission changes can be utilized in information encryption and anti-counterfeiting. Our findings expand the understanding of how the local coordination structure influences the photophysical mechanism in Sb^{3+}-doped OIHMHs and provide a novel method to control the STEs emission.

Materials and methods

Materials

Diantimony trioxide (Sb_2O_3, SP, Macklin), Indium (III) oxide (In_2O_3, 99.99%, Meryer), Hydrochloric acid (HCl, AR, Chongqing Chuandong Chemical), Histamine dihydrochloride ($C_5H_{11}N_3Cl_2$, 98%, Meryer), Ethanol (99.8%, Boer) and Polymethyl methacrylate (PMMA, Sigma Corp) were used without any further purification.

Synthesis of $C_{10}H_{22}N_6InCl_7{\cdot}H_2O$

In_2O_3 (0.069 g, 0.25 mmol) and histamine dihydrochloride (0.368 g, 2.0 mmol) were dissolved in 1.0 mL HCl solution and then filtered into a 20 mL vial to form a clear precursor solution. Then, the vial was placed in a 100 mL vial with 60 mL EtOH inside. The as-prepared solution was sealed and left to stand for ~3 days to afford pale block crystals.

Synthesis of $C_5H_{11}N_3SbCl_5$

Sb_2O_3 (0.138 g, 0.5 mmol) and histamine dihydrochloride (0.184 g, 1.0 mmol) in 1 mL HCl solution and then filtered into a 20 mL vial to form a clear precursor solution. Then, the vial was placed in a 100 mL vial with 60 mL EtOH inside. The as-prepared solution was sealed and left to stand for ~3 days to afford pale block crystals.

Synthesis of $C_{10}H_{22}N_6In_{1-x}Sb_xCl_7{\cdot}H_2O$

For the synthesis of $C_{10}H_{22}N_6In_{1-x}Sb_xCl_7{\cdot}H_2O$,

Sb_2O_3/In_2O_3 aqueous solutions with designed compositions were used and the other conditions were kept invariable to obtain the corresponding crystals.

Characterizations

Single crystal XRD (calculated XRD) was carried out on a microfocal spot X-ray single crystal diffractometer (SuperNova, Agilent Technologies, Poland). The powder X-ray diffraction (XRD) patterns were measured using a Cu Kα radiation (XRD-6100, SHIMADZU, Japan). UV-vis Absorption spectra were collected on a UV-vis spectrophotometer (UV-vis: UV-3600, SHIMADZU, Japan). The steady and transient state PL spectroscopies were measured by a fluorescence spectrometer (FLS1000, Edinburgh Instruments Ltd., England). XPS spectra were collected from an ESCA Lab220I-XL. Raman spectra were collected from LabRAM HR Evolution. SEM and EDS mapping were collected from Jieke TESCAN MIRA LMS.

First-principles calculations

The electronic band structures and wave functions of $C_{10}H_{22}N_6InCl_7{\cdot}H_2O$, Sb^{3+} doped $C_{10}H_{22}N_6InCl_7{\cdot}H_2O$, Sb^{3+} doped $C_{10}H_{22}N_6InCl_7$ and $C_5H_{11}N_3SbCl_5$ were calculated using density functional theory (DFT) implemented on the Vienna ab initio simulation package (VASP). Generalized gradient approximation (GGA) of Perdew-Burke-Ernzerhof (PBE) exchange-correlation functional and pseudopotential with the projector augmented wave (PAW) method were used. The kinetic energy cutoff was set as 400 eV. The electronic wave function was self-consistently converged with energy variation criteria of 10^{-5} eV. The atomic structure was relaxed with 2 × 2 × 4 Gamma-center k-point mesh and the atomic force criteria of 0.005 eV/Å. The density of states (DOS) and orbital-resolved partial densities of states (PDOS) were obtained by sampling the Brillouin zone with 2 × 2 × 4 Gamma-center k-point mesh and Gaussian smearing width of 0.05 eV. Band structures are calculated along high symmetry lines of crystal structure with space group $P2_1/c$ and $P2_1/n$, based on which transition dipole moments are calculated using VASPKIT.

Results and discussion

$C_{10}H_{22}N_6InCl_7{\cdot}H_2O$ single crystals were prepared using an antisolvent diffusion method with $C_5H_{11}N_3Cl_2$ and In_2O_3 in an aqueous solution of hydrochloric acid (HCl) and ethanol as a slowly-diffusing antisolvent. $C_{10}H_{22}N_6InCl_7{\cdot}H_2O$ crystalizes in a monoclinic $P2_1/c$ space group, and the structure features In-Cl octahedral units coordinated by six chlorine atoms, as shown in Fig. 1(a) and Table S1. Furthermore, the crystal structure exhibits a hydrogen bonding network among H_2O molecules, $C_5H_{11}N_3^{2+}$ cation and $[InCl_6]^{3-}$ octahedral unit (Fig. S1). As shown in Fig. S2, the obtained powder X-ray diffraction (PXRD) pattern matches well with the simulated pattern, confirming the high crystal purity.

Under 365 nm excitation, $C_{10}H_{22}N_6InCl_7{\cdot}H_2O$ exhibits its blue emission with a PLQY of 9.8% and a corresponding photoluminescence (PL) peak at ~430 nm (Fig. S3). What's more, the PL decay curve of $C_{10}H_{22}N_6InCl_7{\cdot}H_2O$ can be fitted with a single exponential function, yielding an average lifetime of 1.8 μs (Fig. S4). To confirm the origin of blue emission, we synthesized the organic hydrochloride counterpart, i.e., $C_5H_{11}N_3Cl_2$. The $C_5H_{11}N_3Cl_2$ crystals also show a blue emission centered at 425 nm with a PL lifetime of 1.5 μs (Fig. S5). Thus, it can be reasonably inferred that $C_{10}H_{22}N_6InCl_7{\cdot}H_2O$ and $C_5H_{11}N_3Cl_2$ crystals possess a same phosphorescent mechanism, resulting from the $C_5H_{11}N_3^{2+}$ organic cation.

Doping is an effective strategy for introducing outstanding photoelectric properties in semiconductor materials. By partially replacing In_2O_3 with Sb_2O_3, a series of Sb^{3+} doped $C_{10}H_{22}N_6InCl_7{\cdot}H_2O$ crystals were successfully synthesized. Figure 1(b) illustrates that the $C_{10}H_{22}N_6In_{1-x}Sb_xCl_7{\cdot}H_2O$ crystals appear as colorless under visible light, resembling the original $C_{10}H_{22}N_6InCl_7{\cdot}H_2O$. As the Sb content gradually increases from 0 to 30%, $C_{10}H_{22}N_6In_{1-x}Sb_xCl_7{\cdot}H_2O$ shows an intense green emission. Subsequently, the photophysical properties of the samples at room temperature were thoroughly investigated. In Fig. 1(c), the PLQY data for the series of samples are plotted as a function of the content of Sb. It is observed that all Sb-doped samples have a higher PLQY than that of the undoped compounds, $C_{10}H_{22}N_6InCl_7{\cdot}H_2O$ and $C_5H_{11}N_3SbCl_5$. The incorporated of Sb^{3+} ions enable the formation of $[SbCl_6]^{3-}$ octahedra, which serve as active emission centers in doped crystals. It has been reported that the $[SbCl_6]^{3-}$ octahedra correspond to efficient STEs emission with high PLQY[23,24]. Therefore, in this work, the incorporation of Sb^{3+} dopants results in the increase of PLQY up to 80%, and the PLQY value is found to reduce when incorporating a large amount of Sb dopants, which is ascribed to concentration quenching[25,26]. $C_5H_{11}N_3SbCl_5$ crystalizes

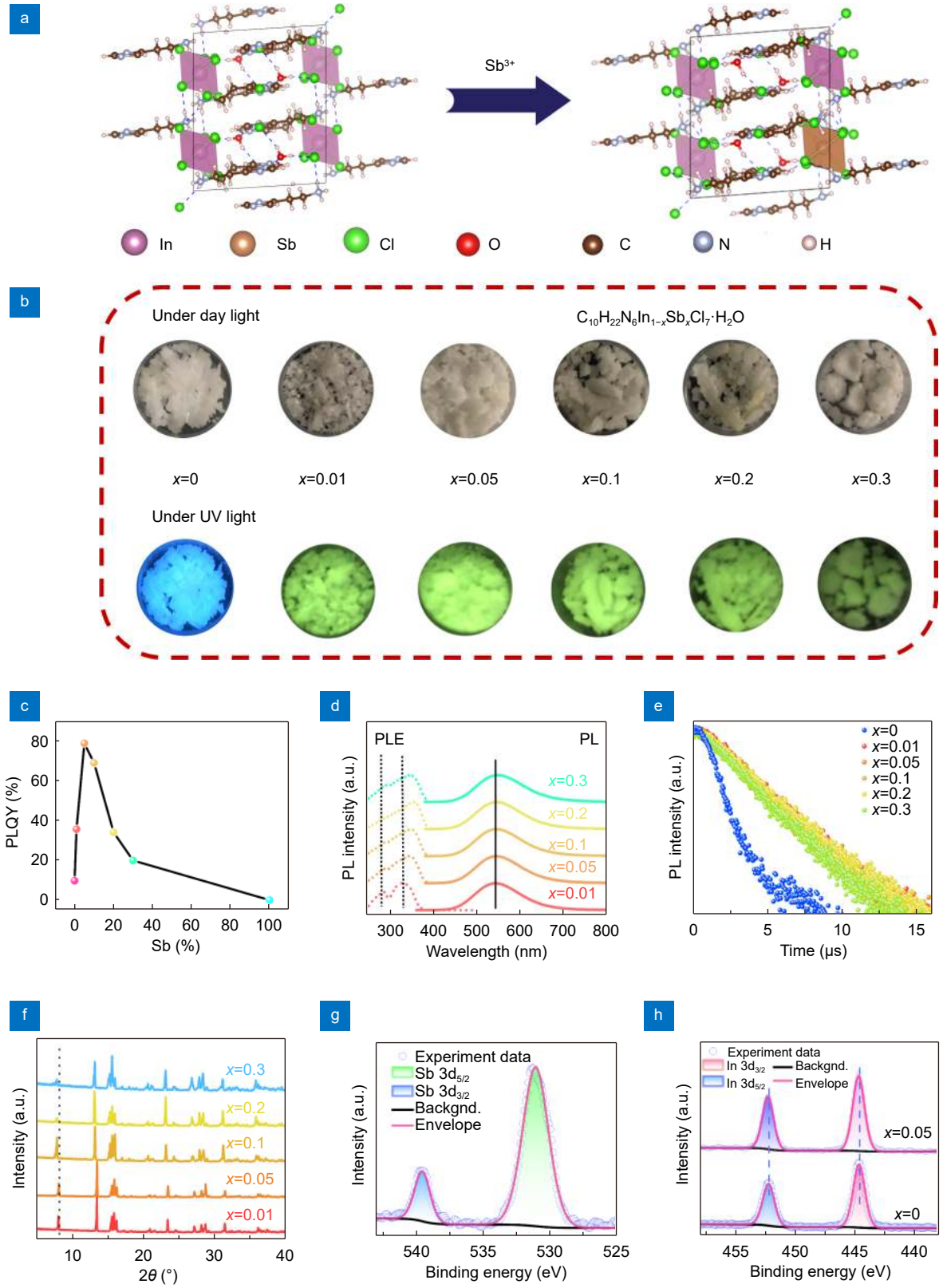

Fig. 1 | (**a**) Crystal structures of undoped and Sb^{3+}-doped $C_{10}H_{22}N_6InCl_7·H_2O$. (**b**) Photographs of $C_{10}H_{22}N_6In_{1-x}Sb_xCl_7·H_2O$ under day light and UV light. (**c**) PLQY, (**d**) Normalized PLE and PL spectra, (**e**) PL decay curve, (**f**) Powder XRD patterns of $C_{10}H_{22}N_6In_{1-x}Sb_xCl_7·H_2O$. (**g**) XPS spectra of Sb 3d in $C_{10}H_{22}N_6In_{0.95}Sb_{0.05}Cl_7·H_2O$. (**h**) XPS spectra of In 3d in pristine $C_{10}H_{22}N_6InCl_7·H_2O$ and $C_{10}H_{22}N_6In_{0.95}Sb_{0.05}Cl_7·H_2O$.

in the monoclinic $P2_1/n$ space group, forming a 1D organic-inorganic hybrid halides (Fig. S6). $C_5H_{11}N_3SbCl_5$ has a PL spectrum with broadband characteristics with dominant peaks at 437 nm and 593 nm (Fig. S7). $C_5H_{11}N_3SbCl_5$ exhibits a low PLQY due to the short distance between Sb ions. The introduction of Sb^{3+} into $C_{10}H_{22}N_6InCl_7{\cdot}H_2O$ results in a strong green emission centered at 545 nm (Fig. 1(d)). As the amount of Sb was increased, the emission wavelength of $C_{10}H_{22}N_6In_{1-x}Sb_xCl_7{\cdot}H_2O$ remained constant (Table S2). Additionally, the photoluminescence excitation (PLE) spectra showed two primary peaks which are assigned to the characteristic $^1S_0$ to $^1P_1$ and $^3P_1$ transitions of Sb^{3+}, respectively. Sb-doping induces an impurity level in the bandgap, leading a reduced bandgap. The PLE spectra shows a redshift trend with increasing the Sb^{3+} concentration due to the Sb-Sb interaction which results in a further reduction of the band gap. As shown in Figs. 1(e) and S8, the PL decay curves for both the doped samples were fitted using a single-exponential function, revealing an average lifetime of 4.3 μs for the doped samples, suggesting that the origin of Sb^{3+} emission.

As illustrated in Fig. 1(f), all the samples exhibit similar XRD patterns. The small shifts towards lower angles observed in these patterns are attributed to the expansion of crystal lattice in doped samples, where the band length of Sb-Cl (1.11 Å) is shorter than that of In-Cl (1.38 Å) [27]. The successful introduction of Sb dopants into the crystal can be verified through the X-ray photoelectron spectra (XPS) (Fig. S9). As illustrated in Fig. 1(g), the peaks observed at 539.5 and 531.0 eV are attributed to the Sb $3d_{3/2}$ and Sb $3d_{5/2}$ components, respectively. The observation of these peaks serves as a clear confirmation of the presence of Sb in the sample. Furthermore, the introduction of Sb^{3+} results in the shifting of two characteristic peaks of In $3d_{3/2}$ and In $3d_{5/2}$ towards higher binding energies (Fig. 1(h)). Accordingly, both In and Sb in the metal halide frameworks are presented in the form of +3 oxidation state, while Cl is presented in the form of −1 valence state (Fig. S10). As shown in Fig. S11, the energy dispersive spectroscopy (EDS) mapping shows a uniform distribution of In and Sb elements in Sb-doped $C_{10}H_{22}N_6InCl_7{\cdot}H_2O$, implying the uniform doping and negligible element segregation.

To identify the origin of the green emission, we conducted a series of experiments. As $C_{10}H_{22}N_6In_{0.95}Sb_{0.05}Cl_7{\cdot}H_2O$ exhibited the strongest emission, we performed further experiments on this compound. When excitation wavelength increases from 260 to 370 nm, the emission wavelength of $C_{10}H_{22}N_6In_{0.95}Sb_{0.05}Cl_7{\cdot}H_2O$ remains unchanged. Under different excitation wavelength, the unchanged PL spectra and FWHM values of $C_{10}H_{22}N_6In_{1-x}Sb_xCl_7$ indicate that its emission originates from the same excited states (Fig. 2(a))[28–30]. As shown in Fig. 2(b), the PL intensity of $C_{10}H_{22}N_6In_{0.95}Sb_{0.05}Cl_7{\cdot}H_2O$ is directly proportional to the excited power density. This implies that its emission may not originate from defects, as evidenced by the absence of a saturated intensity even at high excitation power density[31].

To gain a better understanding of the origins of the strong green emission observed in $C_{10}H_{22}N_6In_{0.95}Sb_{0.05}Cl_7{\cdot}H_2O$, we conducted temperature-dependent PL spectra measurements (Fig. 2(c)). The PL intensity of green emission centered at 545 nm gradually increases when temperature decreases from 300 K to 80 K, which is attributed to the decreased occurrence of nonradiative transitions at the lower temperatures. Figure 2(d) displays the integrated photoluminescence intensity of $C_{10}H_{22}N_6In_{0.95}Sb_{0.05}Cl_7{\cdot}H_2O$ at varying temperatures. Therefore, we calculated the binding energy (E_a) of the STEs using the Arrhenius equation presented below[32]:

$$I(T) = \frac{I_0}{1 + Ae^{(-E_a/k_BT)}}, \tag{1}$$

where I_0 represents the integrated PL intensity at 0 K, k_B denotes the Boltzmann constant and A refers to the pre-exponential coefficient. The binding energy of $C_{10}H_{22}N_6In_{0.95}Sb_{0.05}Cl_7{\cdot}H_2O$ was calculated to be 99.1 meV, as shown in Fig. 2(d). This value is larger than that of traditional 3D perovskites (20–40 meV)[33–35]. The calculated E_a is greater than the thermal ionization energy (~26 meV at 300 K), indicating that excitons can remain stable at room temperature. The substantial exciton binding energy contributes to intense radiative recombination, resulting in a high PLQY. We evaluated the electron-phonon coupling effect by examining the relationship between the FWHM of photoluminescence and temperature (Fig. 2(e)). Moreover, we calculate the Huang-Rhys factor (S) and phonon frequency ($\hbar\omega_{phonon}$) using the following formula[36]:

$$FWHM = 2.36\sqrt{S}\hbar\omega_{phonon}\sqrt{\coth\frac{\hbar\omega_{phonon}}{2k_BT}}, \tag{2}$$

where k_B denotes the Boltzmann constant and T refers to temperature. The calculated S value and phonon

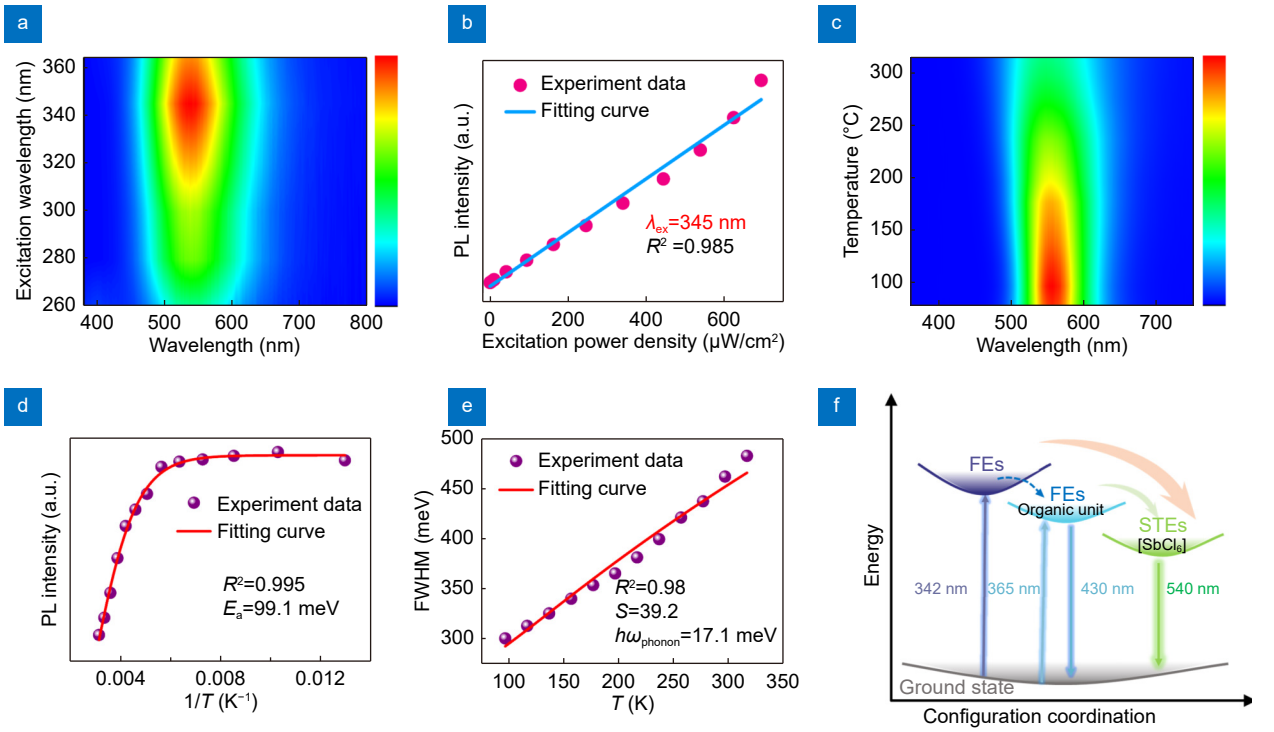

Fig. 2 | (**a**) PL of $C_{10}H_{22}N_6In_{0.95}Sb_{0.05}Cl_7{\cdot}H_2O$ under different excitation wavelengths. (**b**) PL intensity of $C_{10}H_{22}N_6In_{0.95}Sb_{0.05}Cl_7{\cdot}H_2O$ as a function of excitation powers. (**c**) PL spectra of $C_{10}H_{22}N_6In_{0.95}Sb_{0.05}Cl_7{\cdot}H_2O$ under different temperatures. (**d**) Fitting curve between integrated PL intensity of $C_{10}H_{22}N_6In_{0.95}Sb_{0.05}Cl_7{\cdot}H_2O$ and temperature. (**e**) The correlation between FWHM of the $C_{10}H_{22}N_6In_{0.95}Sb_{0.05}Cl_7{\cdot}H_2O$ and temperature. (**f**) Schematic diagram of the photophysical processes.

frequency are found to be 39.2 and 17.1 meV, respectively, indicating a strong electron-phonon coupling that can easily generate STEs for $C_{10}H_{22}N_6In_{0.95}Sb_{0.05}Cl_7{\cdot}H_2O$. Therefore, the emission mechanism of STEs was confirmed due to the features such as microsecond decay time, large Stokes shift, strong electron-phonon coupling, and broadband emission. Figure 2(f) shows the potential emission mechanism of $C_{10}H_{22}N_6In_{1-x}Sb_xCl_7{\cdot}H_2O$. Upon excitation with UV light, the electrons can jump from the ground state to the excited state and subsequently undergo intersystem crossing from a singlet state to a triplet self-trapped state caused by lattice distortion, which results in an effective green emission.

The stability of $C_{10}H_{22}N_6In_{0.95}Sb_{0.05}Cl_7{\cdot}H_2O$ were investigated. As illustrated in Fig. S12, the PL intensity remains almost unchanged when the samples were irradiated for 420 min under a 365 nm UV irradiation. Figure. S13 shows the PL intensity of the $C_{10}H_{22}N_6In_{0.95}Sb_{0.05}Cl_7{\cdot}H_2O$, which retains more than 95% of its original PL intensity even upon heating at 80 °C for 420 minutes. After storing the $C_{10}H_{22}N_6In_{0.95}Sb_{0.05}Cl_7{\cdot}H_2O$ crystals in atmosphere for 30 days, their XRD patterns don't show obvious change compared with preparing ones, and their emission intensity maintains 90% of the initial value (Fig. S14). All of the above results indicate the good stability of synthesized samples.

As reported by previous studies, Sb^{3+}-doped hybrid metal halides predominantly emit yellow or red light[36–38]. The green light emission of the samples may result from a robust hydrogen bond network that influences the distortion of the $[SbCl_6]^{3-}$ polyhedron's excited state structure, thereby retaining it at a higher excited state energy level and emitting green light. The thermogravimetric analysis (TGA) curve shows a weight loss from 25 to 140 °C for $C_{10}H_{22}N_6In_{0.95}Sb_{0.05}Cl_7{\cdot}H_2O$, correlating with the loss of H_2O in the structure (Fig. S15). After removing the water molecules, $C_{10}H_{22}N_6In_{0.95}Sb_{0.05}Cl_7$ underwent a red shift in PL emission, resulting in yellow emission, as shown in Fig. 3(a). After heating, the emission wavelength of $C_{10}H_{22}N_6In_{0.95}Sb_{0.05}Cl_7{\cdot}H_2O$ increased from 540 to 570 nm, as depicted in the Fig. 3(b) and 3(c). The breaking of the hydrogen bond network and the existence of larger excited state structural changes of the molecule are responsible for the observed phenomenon. Removing water molecules caused a larger degree of excited state structural distortion of the molecule, which created deeper energy levels of STEs level. This is

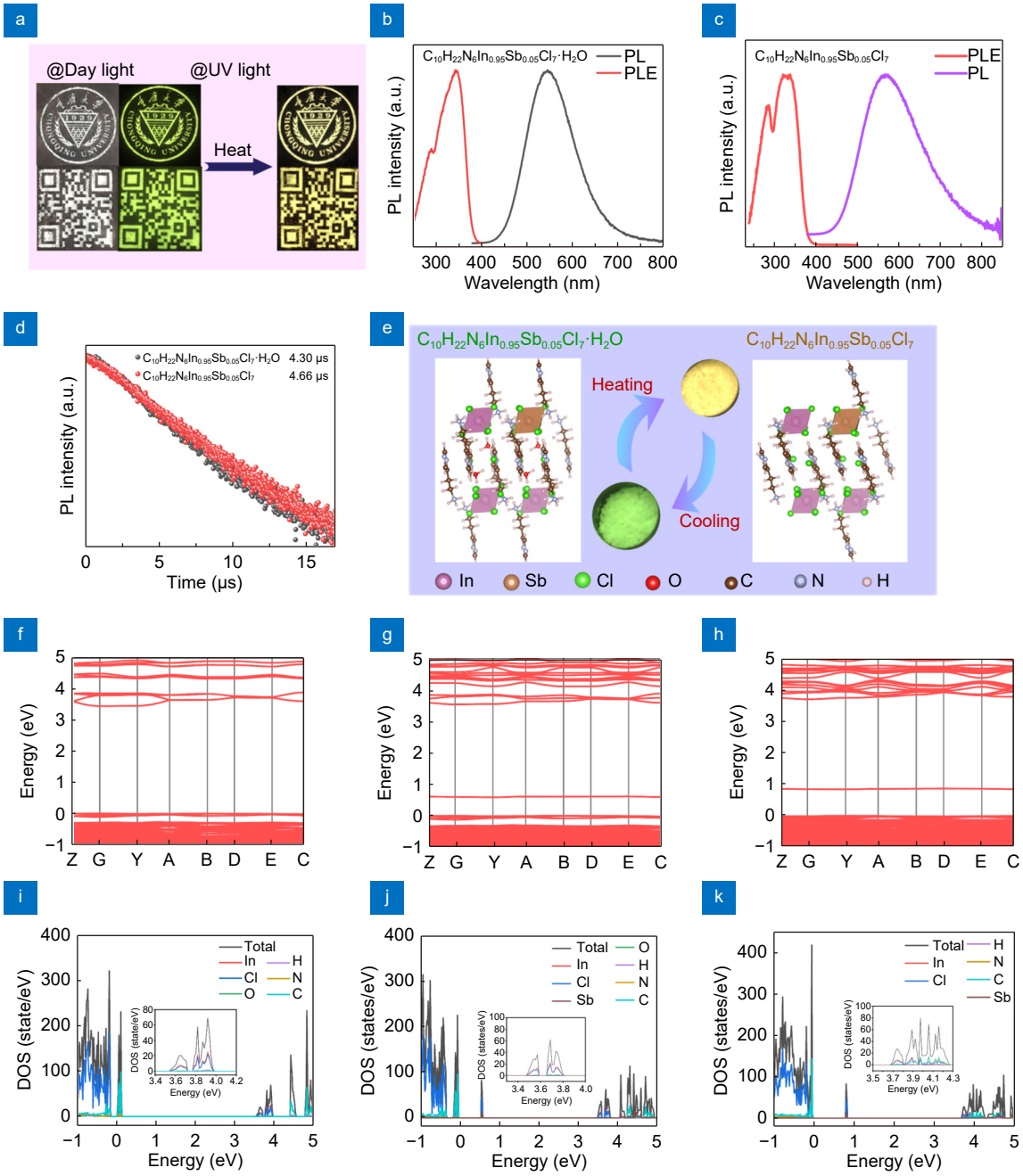

Fig. 3 | (**a**) Patterned images of $C_{10}H_{22}N_6In_{0.95}Sb_{0.05}Cl_7·H_2O$ and $C_{10}H_{22}N_6In_{0.95}Sb_{0.05}Cl_7$ under day light and UV light. Normalized PLE spectra and PL spectra of (**b**) $C_{10}H_{22}N_6In_{0.95}Sb_{0.05}Cl_7·H_2O$ and (**c**) $C_{10}H_{22}N_6In_{0.95}Sb_{0.05}Cl_7$. (**d**) PL decay curve of $C_{10}H_{22}N_6In_{0.95}Sb_{0.05}Cl_7·H_2O$ and $C_{10}H_{22}N_6In_{0.95}Sb_{0.05}Cl_7$. (**e**) The crystal structure of Sb^{3+}-doped $C_{10}H_{22}N_6InCl_7·H_2O$ before and after heating. DFT electronic structures of (**f**) $C_{10}H_{22}N_6InCl_7·H_2O$, (**g**) Sb^{3+}-doped $C_{10}H_{22}N_6InCl_7·H_2O$ and (**h**) Sb^{3+}-doped $C_{10}H_{22}N_6InCl_7$. Density of states of (**i**) $C_{10}H_{22}N_6InCl_7·H_2O$, (**j**) Sb^{3+}-doped $C_{10}H_{22}N_6InCl_7·H_2O$ and (**k**) Sb^{3+}-doped $C_{10}H_{22}N_6InCl_7$.

evidenced by the increase of PL lifetime from 4.3 μs to 4.66 μs due to the greater excited state distortion (Fig. 3(d)). Due to dominant STEs mechanism in Sb^{3+}-doped $C_{10}H_{22}N_6InCl_7·H_2O$, its emission properties can be modulated by excited states induced from distorted structures. After removing the water molecules and breaking the hydrogen bond networks, the Raman intensity of A_{1g} increases (Fig. S16), corresponding to larger structural distortion. As a result, red shifts of PL spectra and longer PL lifetime are found in Fig. 3(b–d). Additionally, the $C_{10}H_{22}N_6In_{0.95}Sb_{0.05}Cl_7·H_2O$ displayed a change in luminescence from yellow to green after absorbing water molecules, which suggests that the process was reversible. Density functional theory (DFT)

theoretical calculations revealed that when water molecules were removed, the degree of distortion of $[SbCl_6]^{3-}$ octahedra in the calculated crystal structure was altered (Fig. 3(e)). The distortion degree of the $[SbCl_6]^{3-}$ octahedrons is evaluated using equation[38–40]:

$$\lambda_{oct} = \frac{1}{6}\sum_{i=1}^{6}\left[\frac{d_i - d_0}{d_0}\right]^2, \quad (3)$$

where d_0 is the average Sb-Cl bond length, di are the six individual Sb-Cl bond lengths. The λ_{oct} of Sb^{3+} doped $C_{10}H_{22}N_6InCl_7{\cdot}H_2O$ is 3.13×10^{-4}, while the corresponding values of Sb^{3+} doped $C_{10}H_{22}N_6InCl_7{\cdot}H_2O$ is 9.22×10^{-4} due to the breaking of the hydrogen bond network.

To further investigate the optoelectronic properties of undoped and Sb^{3+} doped $C_{10}H_{22}N_6InCl_7{\cdot}H_2O$, we analyzed the band structures through the DFT framework. The crystal structure used in the theory calculation is depicted in Fig. S17. The formation of STEs generally requires low electronic dimensionality. Figure 3(f–h) depict the nearly flat conduction band (CB) and valence band (VB) of undoped and Sb^{3+}-doped $C_{10}H_{22}N_6InCl_7{\cdot}H_2O$, as well as Sb^{3+}-doped $C_{10}H_{22}N_6InCl_7$, indicating a high degree of electronic state localization that promotes STE formation. After introducing Sb^{3+} ions, the bandgap of the sample decreased from 3.41 eV to 2.90 eV, attributed to the introduction of Sb ion level. This corresponds to the red shift observed in their PLE spectra. After removing water molecules, the bandgap of the sample was 2.83 eV, which may also lead to red shift in luminescence. $C_5H_{11}N_3SbCl_5$ shows a lower bandgap of 2.58 eV compared to $C_{10}H_{22}N_6InCl_7{\cdot}H_2O$, as presented in Fig. S18. As shown in the total and orbital-resolved partial density of states, both the top of valance bands is derived from C and N orbitals, while the bottom of conduction band is dominated by In and Cl orbitals for $C_{10}H_{22}N_6InCl_7{\cdot}H_2O$ (Fig. 3(i)). Figure 3(j, k) depict that the valence band maximum consists primarily of Sb and Cl states, while the conduction band minimum has a mixed character of In and Cl for both Sb^{3+}-doped $C_{10}H_{22}N_6InCl_7{\cdot}H_2O$ and Sb^{3+}-doped $C_{10}H_{22}N_6InCl_7$.

Based on its unique optical properties, an anticounterfeiting label was fabricated using the as-synthesized $C_{10}H_{22}N_6In_{0.95}Sb_{0.05}Cl_7$. To preventing from water, $C_{10}H_{22}N_6In_{0.95}Sb_{0.05}Cl_7$ was coated in PMMA. As shown in Fig. 4(a), the flowers were coated by $C_{10}H_{22}N_6In_{0.95}Sb_{0.05}Cl_7$@PMMA, while the butterfly and bee were coated by $C_{10}H_{22}N_6In_{0.95}Sb_{0.05}Cl_7$. Both the butterfly and bee emit a yellow emission under 365 nm irradiation before absorbing water and turn to green emission upon 365 nm excitation after absorbing water molecules. An information encryption model, representing "8888 ", was constructed by combining $C_{10}H_{22}N_6InCl_7{\cdot}H_2O$, $C_{10}H_{22}N_6In_{0.95}Sb_{0.05}Cl_7$ and $C_{10}H_{22}N_6In_{0.95}Sb_{0.05}Cl_7$@PMMA. As shown in Fig. 4(b), the fake number information "8888" is apparent under daylight. Upon excitation with 365 nm UV light, referred to as the first decryption, another fake information "1929" in the template emerges. However, the actual information of "1525" can be observed under 365 nm excitation after absorbing water molecules. As shown in Fig. 4(c), the water-responsive photoluminescent behaviors of $C_{10}H_{22}N_6In_{0.95}Sb_{0.05}Cl_7$ and $C_{10}H_{22}N_6In_{0.95}Sb_{0.05}Cl_7$@PMMA was utilized to construct a dual-input logic gate. According to Fig. 4(d), input A is defined as the sampling signal, with $C_{10}H_{22}N_6In_{0.95}Sb_{0.05}Cl_7$ represented as "1 " and $C_{10}H_{22}N_6In_{0.95}Sb_{0.05}Cl_7$@PMMA represented as "0". Additionally, input B was designated as the environmental signal, where the process of water absorption is represented as "1" and the absence of water absorption is represented as "0 ". For the output signal, we defined green emission as "1" and yellow emission as "0". The logical gate will only be activated when both input A and B are 1, which corresponds to the green emission of the samples after absorbing water molecules. It is worth noting that this doping strategy is applicable to other compounds, providing a new direction for designing optical encryption applications.

Conclusions

In summary, we synthesized $C_{10}H_{22}N_6InCl_7{\cdot}H_2O$ and Sb^{3+} doped $C_{10}H_{22}N_6InCl_7{\cdot}H_2O$ using an antisolvent diffusion method. Sb^{3+} doped $C_{10}H_{22}N_6InCl_7{\cdot}H_2O$ shows strong broadband green light emission peaking at 540 nm and a high PLQY of 80%. The hydrogen bond network limits the structural distortion of the excited state of the inorganic cluster , which plays an important role in the emission of Sb^{3+} doped $C_{10}H_{22}N_6InCl_7{\cdot}H_2O$. Breaking the hydrogen bond network causes Sb^{3+}-doped $C_{10}H_{22}N_6InCl_7{\cdot}H_2O$ to emit a yellow light. Therefore, the pattern based on transformed Sb^{3+}-doped $C_{10}H_{22}N_6InCl_7{\cdot}H_2O$ has been achieved and applied in the digital encryption and decryption as well as optical logical "AND" gate. Our findings expand the understanding

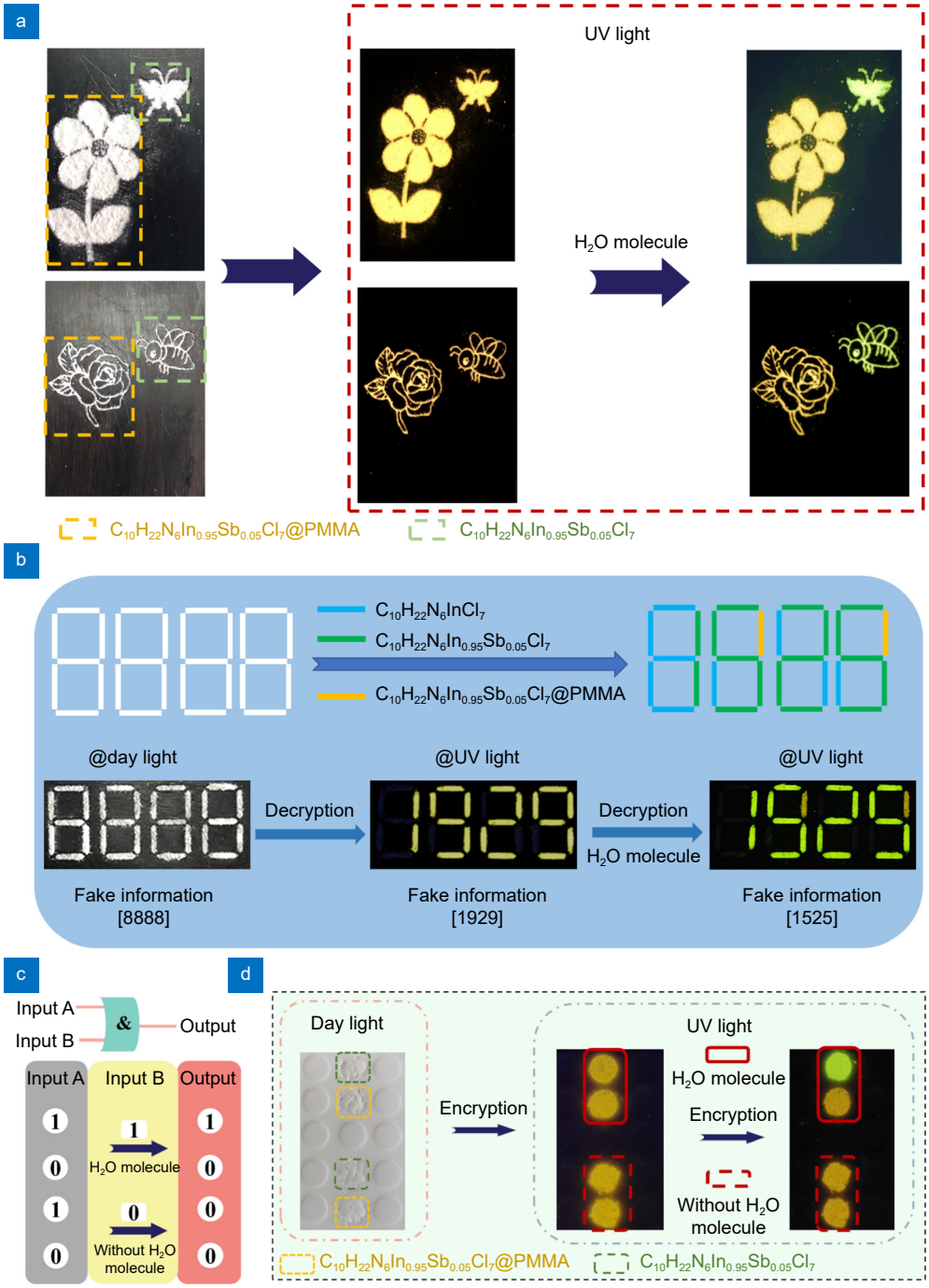

Fig. 4 | (**a**) Photographs of patterns composed of $C_{10}H_{22}N_6In_{0.95}Sb_{0.05}Cl_7$and $C_{10}H_{22}N_6In_{0.95}Sb_{0.05}Cl_7$@PMMA. (**b**) Information encryption process produced by $C_{10}H_{22}N_6In_{0.95}Sb_{0.05}Cl_7{\cdot}H_2O$ and $C_{10}H_{22}N_6In_{0.95}Sb_{0.05}Cl_7{\cdot}H_2O$ @PMMA. (**c**) Design of optical AND logical gate produced by $C_{10}H_{22}N_6In_{0.95}Sb_{0.05}Cl_7{\cdot}H_2O$ and $C_{10}H_{22}N_6In_{0.95}Sb_{0.05}Cl_7{\cdot}H_2O$ @PMMA. (**d**) The experimental demonstration of optical AND logical gate.

of how the local coordination structure influences the photophysical mechanism in Sb^{3+}-doped metal halides and provide a novel method to control the STE emission.

References

1. Liu H, Shonde TB, Gonzalez F et al. Efficient red light emitting diodes based on a zero-dimensional organic antimony halide hybrid. *Adv Mater* **35**, 2209417 (2023).
2. Kingsford RL, Jackson SR, Bloxham LC et al. Controlling phase transitions in two-dimensional perovskites through organic cation alloying. *J Am Chem Soc* **145**, 11773–11780 (2023).
3. Zhang Y, Zhang YG, Zhao YY et al. Crystal-liquid-glass transition and near-unity photoluminescence quantum yield in low melting point hybrid metal halides. *J Am Chem Soc* **145**, 12360–12369 (2023).
4. Yang CH, Xiao SB, Xiao H et al. Efficient red-emissive circularly polarized electroluminescence enabled by quasi-2D per-

ovskite with chiral spacer cation. *ACS Nano* **17**, 7830–7836 (2023).
5. Dryzhakov B, Lawrie BJ, Celio JZ M et al. Dual emission bands of a 2D perovskite single crystal with charge transfer state characteristics. *ACS Nano* **17**, 12200–12207 (2023).
6. Tian Y, Peng H, Wei QL et al. Moisture-induced reversible structure conversion of zero-dimensional organic cuprous bromide hybrids for multiple photoluminescent anti-counterfeiting, information encryption and rewritable luminescent paper. *Chem Eng J* **458**, 141436 (2023).
7. Pareja-Rivera C, Morán-Muñoz JA, Gómora-Figueroa AP et al. Optimizing broadband emission in 2D halide perovskites. *Chem Mater* **34**, 9344–9349 (2022).
8. Song ZX, Jia ZL, Guo XY et al. Chirality–racemization strategy toward copper (I) iodide hybrid single‐crystalline scintillators for X‐ray detection and imaging applications. *Adv Opt Mater* **11**, 2203014 (2023).
9. Su BB, Jin JC, Han K et al. Ceramic wafer scintillation screen by utilizing near‐unity blue‐emitting lead‐free metal halide $(C_8H_{20}N)_2Cu_2Br_4$. *Adv Funct Mater* **33**, 2210735 (2023).
10. Xu TT, Li YY, Nikl M et al. Lead-free zero-dimensional organic-copper(I) halides as stable and sensitive x-ray scintillators. *ACS Appl Mater Interfaces* **14**, 14157–14164 (2022).
11. Liang DH, Sun Z, Lu SR et al. Solvent-free grinding synthesis of hybrid copper halides for white light emission. *Inorg Chem* **62**, 7296–7303 (2023).
12. Liang DH, Xiao HB, Cai WS et al. Mn^{2+}‐based luminescent metal halides: syntheses, properties, and applications. *Adv Opt Mater* **11**, 2202997 (2023).
13. Ma W, Liang DH, Qian QK et al. Near-unity quantum yield in zero-dimensional lead-free manganese-based halides for flexible X-ray imaging with high spatial resolution. *eScience* **3**, 100089 (2023).
14. Liu XH, Li XL, Li J et al. Modulating anthracene excimer through guest engineering in two-dimensional lead bromide hybrids. *Inorg Chem Front* **10**, 2917–2925 (2023).
15. Liao JF, Zhang ZP, Wei JH et al. Emission‐color‐tunable Pb−Sn alloyed single crystals with high luminescent efficiency and stability. *Adv Opt Mater* **10**, 2102426 (2022).
16. Zhang ZP, Liao JF, Xing GC. Regulating the coordination geometry of polyhedra in zero-dimensional metal halides for tunable emission. *Nanoscale* **15**, 5241–5248 (2023).
17. Li ZY, Li Y, Liang P et al. Dual-band luminescent lead-free antimony chloride halides with near-unity photoluminescence quantum efficiency. *Chem Mater* **31**, 9363–9371 (2019).
18. Liao JF, Zhang ZP, Wang BZ et al. Full-color-tunable phosphorescence of antimony-doped lead halide single crystal. *npj Flex Electron* **6**, 57 (2022).
19. Liu KJ, Hao SQ, Cao JD et al. Antimony doping to enhance luminescence of tin(IV)-based hybrid metal halides. *Inorg Chem Front* **9**, 3865–3873 (2022).
20. Lin WC, Wei QL, Huang T et al. Antimony doped tin(IV) hybrid metal halides with high-efficiency tunable emission, WLED and information encryption. *J Mater Chem C* **11**, 5688–5700 (2023).
21. Wu JJ, Li XL, Lian X et al. Ultrafast study of exciton transfer in Sb(III)-doped two-dimensional $[NH_3(CH_2)_4NH_3]CdBr_4$ perovskite. *ACS Nano* **15**, 15354–15361 (2021).
22. Liang DH, Liu XH, Luo BB et al. High quantum yield of in-based halide perovskites for white light emission and flexible X-ray scintillators. *Ecomat* **5**, e12296 (2023).
23. Cheng XW, Li RF, Zheng W et al. Tailoring the broadband emission in all‐inorganic lead‐free 0D in‐based halides through Sb^{3+} doping. *Adv Opt Mater* **9**, 2100434 (2021).
24. Han PG, Luo C, Yang SQ et al. All-Inorganic lead-free 0D perovskites by a doping strategy to achieve a PLQY boost from <2 % to 90. *Angew Chem Int Ed* **59**, 12709–12713 (2020).
25. Li ZY, Song GM, Li Y et al. Realizing tunable white light emission in lead-free indium(III) bromine hybrid single crystals through antimony(III) cation doping. *J Phys Chem Lett* **11**, 10164–10172 (2020).
26. Chen CH, Xiang JM, Chen YH et al. White-light emission lead-free perovskite phosphor Cs_2ZrCl_6: Sb^{3+}. *Ceram Int* **48**, 1851–1856 (2022).
27. Jing YY, Liu Y, Jiang XX et al. Sb^{3+} dopant and halogen substitution triggered highly efficient and tunable emission in lead-free metal halide single crystals. *Chem Mater* **32**, 5327–5334 (2020).
28. Wei JH, Yu YW, Luo JB et al. Bright cyan-emissive copper(I)-halide single crystals for multi-functional applications. *Adv Opt Mater* **10**, 2200724 (2022).
29. Su BB, Jin JC, Peng YH et al. Zero-dimensional organic copper(I) iodide hybrid with high anti-water stability for blue-light-excitable solid-state lighting. *Adv Opt Mater* **10**, 2102619 (2022).
30. Banerjee D, Popy DA, Leininger BC et al. Zero-dimensional broadband yellow light emitter $(TMS)_3Cu_2I_5$ for latent fingerprint detection and solid-state lighting. *ACS Appl Mater Interfaces* **15**, 30455–30468 (2023).
31. Chen D, Hao SQ, Zhou GJ, Deng CK et al. Lead-free broadband orange-emitting zero-dimensional hybrid $(PMA)_3InBr_6$ with direct band gap. *Inorg Chem* **58**, 15602–15609 (2019).
32. Yangui A, Garrot D, Lauret JS et al. Optical investigation of broadband white-light emission in self-assembled organic–inorganic perovskite $(C_6H_{11}NH_3)_2PbBr_4$. *J Mater Chem C* **119**, 23638–23647 (2015).
33. Yang HZ, Zhang YH, Pan J et al. Room-temperature engineering of all-inorganic perovskite nanocrsytals with different dimensionalities. *Chem Mater* **29**, 8978–8982 (2017).
34. Protesescu L, Yakunin S, Bodnarchuk MI et al. Nanocrystals of cesium lead halide perovskites ($CsPbX_3$, X = Cl, Br, and I): novel optoelectronic materials showing bright emission with wide color gamut. *Nano Lett* **15**, 3692–3696 (2015).
35. Ai B, Liu C, Deng Z et al. Low temperature photoluminescence properties of $CsPbBr_3$ quantum dots embedded in glasses. *Phys Chem Chem Phys* **19**, 17349–17355 (2017).
36. Peng H, Wang XX, Zhang ZH et al. Bulk assembly of a 0D organic tin(II) chloride hybrid with high anti-water stability. *Chem Commun* **57**, 8162–8165 (2021).
37. Wu LK, Li RF, Wen WY et al. Lead-free hybrid indium perovskites with near-unity PLQY and white light emission using an Sb^{3+} doping strategy. *Inorg Chem Front* **10**, 3297–3306 (2023).
38. Shi CM, Xuan HL, Wu Y et al. Tunable luminescence on indium halide hybrid regulated by Sb^{3+} doping concentration. *Adv Opt Mater* **11**, 2202376 (2023).
39. Su BB, Song GM, Molokeev MS et al. Synthesis, crystal structure and green luminescence in zero-dimensional tin halide $(C_8H_{14}N_2)_2SnBr_6$. *Inorg Chem* **59**, 9962–9968 (2020).
40. Li J, Wu JJ, Xiao YH et al. Efficient triplet energy transfer in a 0D metal halide hybrid with long persistence room temperature phosphorescence for time-resolved anti-counterfeiting. *Inorg Chem Front* **10**, 7167–7175 (2023).

Acknowledgements

This work is financially supported by National Natural Science Foundation of China (11974063); Graduate research innovation project, School of Optoelectronic Engineering, Chongqing University (GDYKC2023002); Fundamental Research Funds for the Central Universities (2022CDJQY-010). The authors extend their appreciation to the Deputyship for Research and Innovation, Ministry of Education in Saudi Arabia for funding this research work through the project no. (IFKSUOR3–073–9). The authors would like to thank Dr. Xiangnan Gong and Miss Chuanyao Yang at Analytical and Testing Center of Chongqing University for their assistance with SCXRD and PL analysis.

Author contributions

D. H. Liang, Saif M. H. Qaid, and S. Y. Zhao contributed to the experimental design. D. H. Liang performed the experimental studies. Q. K. Qian performed computational study. D. H. Liang, W. S. Cai, B. B. Luo and Z. G. Zang prepared the manuscript. All authors reviewed and revised the manuscript in several steps and approved the final version of the manuscript.

Competing interests

The authors declare no competing financial interests.

Supplementary information

The authors declare no competing financial interests.
https://doi.org/10.29026/oea.2024.230197

Scan for Article PDF